Experimental and Simulated Temperature Variations in a $LiFePO_4$-20Ah Battery during Discharge Process

S. Panchal[1*], I. Dincer[1], M. Agelin-Chaab[1], R. Fraser[2], and M. Fowler[3]

[1] Department of Automotive, Mechanical & Manufacturing Engineering, Faculty of Engineering & Applied Science, University of Ontario Institute of Technology, 2000 Simcoe Street North, Oshawa, Ontario, Canada, L1H 7K4
[2] Mechanical and Mechatronic Engineering Department, University of Waterloo, 200 University Avenue West, Waterloo, Ontario, Canada, N2L 3G1
[3] Chemical Engineering Department, University of Waterloo, 200 University Avenue West, Waterloo, Ontario, Canada, N2L 3G1
*Corresponding Author's Telephone: +1-519-722-4420,
*Corresponding Author's Email: satyam.panchal@uwaterloo.ca, satyam.panchal@uoit.ca

Abstract

The present study investigates the impact of various discharge rates on the thermal (temperature and heat generation profiles) and electrical performance of the Li-ion battery for electric vehicles and hybrid electric vehicles. For this, a prismatic Li-ion phosphate ($LiFePO_4$) battery with 20 Ah capacity is tested under constant current discharge rates of C/10, C/5, C/2, 1C, 2C, 3C, and 4C and surface temperature and voltage distributions during both charging and discharging are measured. In addition, IR images were also captured during experiments with a Flir Therma CAM S60 IR camera at various discharge rates and are reported in this study. Furthermore, a thermal model is created and validated for a particular battery using a MATLAB Simulink in terms of temperature, voltage, heat generation, and internal resistance. The results of this study demonstrate that the increased C-rates from C/10 to 4C results in increased temperature profiles on the principal surface of the battery. Also, at the lower discharge rates (below 1C), the surface temperature remains close to an ambient temperature, but at higher discharge rates (above 1C); the surface temperature quickly increases for all C-rates. The most noteworthy surface temperature distribution is observed to be 58.1°C towards the end of 4C discharge.

Keywords: Energy, Electric vehicle, Hybrid electric vehicle, Battery, Heat transfer, Temperature.

1. Introduction

Electric vehicles (EVs), hybrid electric vehicles (HEVs), and plug-in hybrid electric vehicles (PHEVs) gives the best arrangement with a specific end goal of dramatically reducing the level of pollution in the environment created by the automotive sector. These vehicles additionally diminish the reliance on petroleum. Today, the li-ion batteries are broadly utilized as rechargeable energy storage systems for EVs, HEVs, and PHEVs due to a number of factors: i) great power densities and specific energy [1]; ii) great nominal voltage and low rate of self-discharge [2] ; and iii) very good cycle-life and no memory effect [3]. Nowadays, portable workstations, phones, toys, radios, laser pointers, slide changers, and numerous

other devices use Li-ion batteries as the primary or auxiliary source of power [4]. In light of their development, a few types of Li-ion batteries are available in the market, for example cylindrical, coin, and prismatic. Cylindrical and coin batteries are generally utilized in small products such as wrist watches, laser pointers, and slide changers [5], with the exception of Tesla Motors which used cylindrical in their vehicles while prismatic batteries are utilized for high capacity rating, for example, in EVs, HEVs, and PHEVs [6]. Battery cell damage can be possible if legitimate safety measures are not taken, for example, surpassing voltage, current or power limits during both charging and releasing. From one perspective, high temperature during charge and release will likewise bring about temperature surpassing reasonable reach, which diminishes the battery execution, even resulting into fire and explosion [7, 8]. Besides, Li-ion batteries should be precisely checked and handled (electrically and thermally) to avoid safety (inflammability) and performance related problems [9, 10, 11]. As a result, battery thermal management (BTM) has turned into a very important research focus in recent years due to its extraordinary necessity [12, 13, 14].

Li-ion battery cell contains five different layers, to be specific: the positive current collector, positive electrode (known as cathode), the negative current collector, negative electrode (known as anode), and the separator. The positive electrode materials [15, 16] can be regularly of four types: 1) a metal oxide with layered structure, for example, lithium cobalt oxide ($LiCoO_2$ / LCO) [17]; $LiCoO_2$: $LiCoO_2$ is the most normally utilized cathode material. Li-ions are intercalated between sheets of CoO_2 is 274 mAh/g, but an anisotropic structural change happens at $Li_{0.5}CoO_2$, so the realizable capacity is limited to about 140-160 mAh/g [18, 19, 20, 21]. The discharge capacity of $LiCoO_2$ is great; 136 mAh/g at a 5C rate has been shown with multiwalled carbon nanotubes (CNT) enlarged cathodes [21]; 2) a metal with a three dimensional spinal structure, for example, lithium manganese oxide ($LiMn_2O_4$) [22]; $LiMn_2O_4$: $LiMn_2O_4$ is a promising cathode material with a cubic spinel structure. In the structure, the corners of each tetrahedral and octahedral are oxygen atoms. The theoretical particular capacity is 148 mAh/g. Current outlines accomplish somewhere around 115 and 130 mAh/g at modest discharge rates of 1C or less [23, 24, 25]; 3) a metal with an olivine structure, for example, lithium iron phosphate ($LiFePO_4$/LFP) [26]. $LiFePO_4$: $LiFePO_4$ is one of the standout amongst the latest cathode materials to be presented. Its olivine structure is altogether different from the layered and spinel structures of other lithium ion chemistries, and its intercalation mechanism is also different, involving phase changes. It also contains a specific capacity (theoretical) of 170 mAh/g, a figure which has been achieved by recent advances [27]; and 4) lithium nickel manganese cobalt oxide ($LiNiMnCoO_2$/NMC). Anode materials are commonly carbonaceous in nature. The material for anode is usually graphite or a metal oxide and commonly used anode materials are graphite and silicon. The electrolyte can be liquid, polymer or solid. The electrolyte is commonly a

lithium salt dissolved in organic solvents. Ordinarily, for Li-ion batteries, in liquid electrolytes, a blend of alkyl carbonates, for example, ethylene carbonate (EC), diethyl carbonate (DEC), ethyl-methyl carbonate (EMC), and also dimethyl carbonate (DMC) is utilized with $LiPF_6$ as the dissolved lithium salt [28].

Battery modeling based on differential equations can give a profound comprehension of the physical and chemical process inside the battery and is helpful when outlining a cell; in any case, high computational time makes these models unreasonable for applications that require several model cycles. A few illustrations are; 1) R_{int} model, the model comprises with OCV (V_{OC}), and two sort of internal resistance to represent for different resistance values under discharging and charging respectively. These two parameters model all types of internal resistance including internal ohmic and polarization resistances. The diodes demonstrate that during charging and discharging only one resistance is used. The battery terminal voltage (V_{batt}) is represented as the OCV in addition to the voltage rise or drop over the resistor. 2) Single RC circuit model, it enhances the R_{int} model by including a resistive-capacitive component. Total battery resistance is given by a combination of charge transfer (R_{ct}), ohmic (R_{ohm}), and diffusion (C_{diff}) resistances. The capacitive component permits the model to simulate time reliant and transient behavior. In the R-RC model, it is difficult to determine the resistance and capacitance values specifically from experimental data. Rather, parameter estimation strategies, for example, genetic algorithms [29], multi-swarm particle swarm optimization [30], or least squares curve fitting are utilized to fit the model to test data [31]. Huria, Ceraolo, Gazzarri, and Jackey [32] looked at a wide range of equivalent circuit models and found that the R-RC model performs well despite its simplicity. 3) Dual RC circuit model is also known as the second-order RC model which adds a second RC component to the single RC circuit model. The second RC component gives more prominent determination of transient behavior by separating concentration polarization and activation polarization effects. Parameterizing the dual RC model is like the single RC model – the same parameter estimation algorithms can be utilized, however computational expense will be higher because of the extra variables. The dual RC model is more exact than the single RC model, and both are appropriate for system level battery modeling [29, 30, 32, 33, 34]. Li-ion battery thermal modeling is additionally imperative for battery originators since it gives helpful data on battery charging/discharging, transient behavior and the health status of the battery (battery degradation) as a function of various stress factors (e.g. temperature, discharge rate). Battery models are additionally utilized for on-line self-learning performance and SOC estimation in BTMS [35, 36, 37]. There are various studies in the open literature on for battery thermal modeling, using different approaches such as artificial neural network (NN) [38, 39, 40, 41], finite element model (FEM) [42] or lumped parameter model (LPM) [43], linear parameter varying (LPV) model [44], or partial differential equation (PDE) model [45].

As a non-invasive method of temperature estimation, infra-red (IR) thermography is a fabulous technique. In the literature many examples exist of researchers utilizing IR thermography to capture thermal gradients. Similarly single or multiple thermocouples have been utilized to validate electro-thermal or chemical models. Keyser and Pesaran in [46] used thermal image of Generation-I (4.5 Ah), Generation-II (5 Ah), Generation-III (8 Ah), lithium polymer cells or batteries to measure heat generation and temperature distribution. The 1st and 2nd generation batteries provided hints of localized heat during IR imaging below the cathode during discharge, whereas the 3rd generation battery remained moderately consistent in temperature. Due to the improved and excellent tabs designed, the 3rd generation turned into the most effective of the batteries tried. Niculuta and Veje in [47], likewise used IR thermography to investigate the temperature distribution on the surface at a discharge of 14A, 35A, and 70A $LiFePO_4$ battery. It was found that the highest temperature measured at surface was 32.1 °C during experiment; the model gave a most extreme value of temperature of 33.5 °C. They also found that with 35A currents (C/2) or greater used to discharge or charge the battery, the profile of temperature is not consistent.

The aim of the present study is to conduct both experimental and simulation studies on the measurements, analysis and assessment of performance of a $LiFePO_4$-20Ah under various discharge rates to provide a unique source of knowledge and information for the researchers to pursue these studies for further in technology development. Here are the specific objectives of this study:

- Design and development of the experimental set-up for battery thermal testing
- Study of the surface temperature profiles at lower and higher discharge rates.
- Experimental measurements of the voltage profiles at lower and higher discharge rates.
- Development of the battery thermal model and validation with the experimental data using MATLAB Simulink.
- To acquire and analyze the IR images at various discharge rates.

2. Experimental Apparatus and Procedure

In this section, the experimental set-up and the methodology are described. A $LiFePO_4$-20Ah Li-ion pouch battery (prismatic) was investigated under different discharge rates and appears in Figure 1 and the cell particulars are shown in Table 1. The schematic of the set-up used for thermal performance of the Li-ion battery appears in Figure 2. The battery cell was placed in a vertical position during all experiments, and the battery set-up appears in Figure 3. The PC provides the essential controls utilizing LabVIEW VI to the controller and load box through RS-232 links, and the power supply with an Ethernet cable. Additionally, the PC offers a graphical user interface (GUI) for the user to monitor the advancement of the experiment. The controller utilizes simple input/output (I/O) signal wiring to communicate with the

relays and measure the battery voltage. The controller transmits the measured battery voltage back to the PC. The PC sets the current or voltage values on the load box and power supply depending on the experiment. The internally measured current of the load box and power supply is transmitted back to the PC. Depending on the PC requests, the power supply or load box will give power to or draw power from the battery, separately. The LabVIEW VI screen shot appears in Figure 4 which represents the real parameters taken during these experiments, for example, battery voltage, charge current, discharge current, and temperature. In the top left corner in Figure 4, there are three battery voltage windows: battery A, B and C (Bat A, Bat B, and Bat C in LABVIEW screen shot), in other words, there is a possibility to connect three Li-ion batteries together in series. Here, but for the current experimental work, we used only one battery, therefore, the solid green light is seen only for Bat A. The maximum voltage was set to 3.6 V and the over voltage protection was set to a value of 4.2 V. In Figure 4, the battery temperature rise measured by thermocouples can also be seen for Bat A. One can also run a different drive cycle which is also shown in the bottom right corner of LABVIEW screen shot in Figure 4. The voltage and current (charge and discharge) window, which states that once the voltage reaches to cut-off voltage then the cycle changes from discharging to charging cycle. Figure 4 also displays the corresponding current window in which, the red color line is for discharging current and the white color line is for charging current. There are two Emergency shutdown (E-stop) buttons in the test stand. One is near the Moto Tron controller and the other is near Li-ion cell.

In the experimental plan, seven distinctive discharge rates were chosen: C/10, C/5, C/2, 1C, 2C, 3C, and 4C. These C-rates (above and below 1C) were particularly selected in order to examine the impact of C-rates on the thermal and electrical performance of a particular Li-ion battery. The charge rate is 1C for all discharge rates. The corresponding current values for all discharge rates are represented in Table 2.

3. Analysis

A MATLAB Simulink block diagram for a thermal model of battery appears in Figure 5. A battery model is created based on information obtained from the experimental data for a Li-ion battery. The acquired data is incorporated into a look up table along with simple algorithms written in MATLAB/Simulink to access the look-up table. The model works by using an input current draw to measure the battery voltage which together gives an estimate of the power required from the system. The instantaneous capacity is then divided by the maximum capacity to achieve the SOC estimate. There are basically four subsystems: i) voltage, ii) internal resistance, iii) heat generation, and iv) temperature calculation.

The first step is to calculate the simulated voltage (V_{sim}) from the discharge current (I_{dchg}) and discharge capacity (Ah), and the function is given as

$$V_{sim} = f\ (I_{dchg}, Ah) \tag{1}$$

This function is extracted by extrapolation method (polynomial). The State of charge (SOC) is also calculated from

$$SOC = 1 - \frac{U}{Ah\ (rated)} \tag{2}$$

where

$$U = \int I_{dchg}\ dt \tag{3}$$

From the test data, both discharging and charging resistances are written as

$$R_{dchg} = \frac{V_{oc} - V_{end\ of\ discharge}}{I_{dchg}} \tag{4}$$

$$R_{Chg} = \frac{V_{end\ of\ charge} - V_{oc}}{I_{Chg}} \tag{5}$$

The internal resistance which is computed based on Ohm's law (covering the voltage drop (difference between open circuit voltage and the actual or measured terminal voltage), is divided by current values, and is calculated by

$$R_{int} = \frac{\Delta V}{I_{dchg}} = \frac{V_{oc} - V_{act}}{I_{dchg}} \tag{6}$$

The heat generation can be discovered in a battery cell which has two primary sources: (i) change in entropy because of electrochemical reactions and (ii) Joule's heating or Ohmic heating [48, 49, 50]. Based on the pair of electrodes, the reaction heat can be of two types; exothermic for discharging, and endothermic for charging. The Joule or Ohmic part of heating is because of the exchange of current at internal resistances [51]. The rate of heat generation can be computed by

$$\dot{Q} = I(V_{oc} - V_{act}) - I\left[T\left(\frac{dV_{oc}}{dT}\right)\right] \tag{7}$$

In Equation (7), the primary term, $I\ (V_{oc} - V_{act})$ is the Joule or Ohmic heat generation and other irreversible effects in the battery cell. The secondary term, $I\ [T(dV_{oc}/dT)]$ is the heat produced or expended in light of the reversible entropy change which is due to electrochemical reactions inside the battery cell. In practical HEV as well as EV current rates, the secondary term for the most part is negligible contrasted with the primary term [52]. After simplification of Equation (7), the rate of heat generation is given by

$$\dot{Q} = I^2R - T\ \Delta S\ \left[\frac{I}{n\ F}\right] \tag{8}$$

where, I is the current and $I > 0$ for discharge, $I < 0$ for charge, (i.e. +Ve value is taken for discharging and –Ve value is taken for charging), R is the resistance, ΔS is the change in entropy, n is the number of flow of electron, and F is the Faraday's constant (96485 Columb/mol).

Anode as well as cathode current collectors create additional Joule or Ohmic heating because of the higher current densities which can occur in prismatic type battery cells. Equation (9) was produced in another work to incorporate two more items that account for the rate of heat generated in the positive and negative tabs at current collector [53].

$$\dot{Q} = I\left(V_{oc} - V_{act} - T\left(\frac{dV_{oc}}{dT}\right)\right) + A_p R_p I_p^2 + A_n R_n I_n^2 \tag{9}$$

In this paper, we used Equation (10) to calculate the Ohmic part of heat and is given below.

$$Q = (I_{dchg})^2 R_{dchg}\, t \tag{10}$$

Based on this heat, the simulated temperature is calculated by

$$T_{sim} = f\,(Q_{sim}\,, I_{dchg}) \tag{11}$$

This function is extracted by extrapolation method (exponential) and is given by

$$T_{sim} = T_{ss}\left[1 + e^{\left(-\frac{Q}{\zeta}\right)}\right] \tag{12}$$

where, T_{ss} is the steady state temperature [54] and was calculated by

$$T_{ss} = 22.0501 * e^{(0.121 * I_{dchg})} \tag{13}$$

and ζ is the heat constant, which is proportional to the discharge current and is written by

$$\zeta = f\,(I_{dchg}) \tag{14}$$

4. Results and Discussion

The main aim of this study was to see the thermal and electrical performance of the battery at low and high discharge rates from EV and HEV points of view. The results obtained from these tests are presented for a specific Li-ion battery at various C-rates of C/10, C/5, C/2, 1C, 2C, 3C, and 4C. Likewise, to check the accuracy of the developed model, the model validation was performed by comparing the test data with the simulated data obtained from MATLAB Simulink in terms of temperature, voltage, heat generation,

and internal resistance. The IR images which were taken during various discharge rates are also reported. In our previous similar studies of work, for battery thermal modeling, we used different approach (artificial neural network) while in this paper we have used MATLAB Simulink [38, 41, 39].

4.1 Surface Temperature Profiles

Figure 6 demonstrates the surface temperature profile during discharging the battery at C/10, C/5, C/2, 1C, 2C, 3C, and 4C against time. For C/10 discharge rate (i.e. for 10 hour discharge), there is no change in the surface temperature of the battery and it remains close to the ambient temperature (lab temperature). This trend is the same for all lower discharge rates (below 1C). Similarly, in Figure 9 (a to d), a comparison between the experimental temperature profile on the battery surface with the profile anticipated by the thermal model of the battery at discharge rates of 1C, 2C, 3C and 4C is demonstrated. The surface temperature profiles are plotted against the battery discharge capacity. Additionally, Figure 10 (a to c) demonstrates a comparison between the experimental temperature profile on the battery surface with the profile anticipated by the thermal model of the battery at discharge rates of C/2, C/5, and C/10. Here, the strong agreement between the test and simulation data displays the robustness and preciseness of the model. The main aim was to study the thermal performance of a particular battery at low and high discharge rates and by comparing the plots, the higher value of temperature is observed for the 4C discharge rate (58.1°C) and the lower value of temperature is observed for the C/10 discharge rate (21.8°C). That is, as the C-rate increases, the surface temperature distribution also increases. It is also observed that at low rates of discharge of C/10, C/5, and C/2 (i.e. below 1C), there is not much change in the surface temperature distributions but rather when the discharge rate is higher (above 1C), the temperature increases. The reason behind this is that joule heating is the dominant effect. The most extreme temperature toward the end of each discharge rates is presented in Table 3. The relative uncertainty results associated with experimental data for a temperature range of 21.2°C to 58.1°C are within the range of 0.49 % ± 29.5%.

4.2 Voltage Profiles

Figure 7 demonstrates the experimental voltage profile during discharging the battery at C/10, C/5, C/2, 1C, 2C, 3C, and 4C against time. Figure 8 shows the charge voltage profiles for all discharge rates considered in this experimental work. The discharge-cycle begins as soon as the charging completes and the battery voltage reaches the cut off voltage. As has been mentioned before, the charging cycle was at 1C. Figure 9 (e to h) demonstrates a comparison between the measured terminal voltage acquired at 1C, 2C, 3C and 4C discharge rates with the profile anticipated by the thermal model of battery. There is good agreement between the test data and the model output data. Additionally, Figure 10 (d to f) demonstrates

a likeness between the actual terminal voltage obtained at C/2, C/5, and C/10 discharge rates with the profile anticipated by the thermal model. The cell charging follows constant current-constant voltage (CC-CV) protocol until the charge voltage is 3.6V and the cell discharging is with the constant current (CC) until cutoff voltage is 2.0V. At lower discharge rates of C/2, C/5, and C/10, the cell potential remains nearby to the cell's open circuit potential (OCP). As the discharge rate increases (1C, 2C, 3C, and 4C), the cell voltage essentially deviates from the OCP because of Ohmic, activation and mass transport losses. The maximum capacity at the end of each discharge rates is displayed in Table 3. It was found that the discharge capacity remains close to 20 Ah provided by the manufacturer's data sheet.

4.3 Heat Generation Rate Profiles

Figure 11 demonstrates a comparison between the measured heat generation rate gathered at 1C, 2C, 3C and 4C discharge rates with the profile anticipated by the thermal model of the battery. All profiles are drawn against the discharge capacity (Ah). The rate of heat generation was calculated by using Equation (10) and it was found that the rate of heat generation increases as the discharge rate progresses from the start of discharge to the end of discharge. It was noted that there is a steady increase in the rate of heat generation from the start of discharge to 80% of the rated capacity, but after that there is a substantial rise in the rate of heat generation. The rate of heat generation was highest at the end of the discharge rate. Overall, the simulated data agrees well with the experimental data which demonstrates the robustness and accuracy of the model.

4.4 Internal Resistance Profiles

Figure 12 shows a comparison between the internal resistances obtained from the experimental data with the profiles predicted by the thermal model of battery at 1C, 2C, 3C and 4C discharge rates and are plotted against the discharge capacity. A steep rise is seen in the first part of the discharge, the internal resistance is almost constant until 17 Ah when a steady increase is observed. The increase appears to become steeper as discharge progresses and is highest just before the end of discharge. Furthermore, it can be seen that the increase in the discharge rate and thus the discharge current causes consistent increase in the internal resistance from the beginning to the end of discharge. Overall, it shows the good agreement between the measured and the simulated values. However, slight discrepancies are observed, and the simulated values are slightly higher than the calculated values. The highest value of the internal resistance was obtained at the end of 1C discharge rate and is 0.08 Ω. The minimum value of the internal resistance was at 4C discharge rate and is close to 0.017 Ω. The trend observed is that increased discharge rates (between 1C, 2C, 3C and 4C) results in decreased internal resistance.

4.5 Thermal Image Results

Figure 14 demonstrates the thermal images of Li-ion pouch cell during the discharging at 4.5C towards the starting, intermediate and end of the discharge cycle and Figure 13 shows the Flir Therma CAM S60 during IR imaging experiments. The camera recorded images at regular 20 second intervals. The battery was placed on a cardboard stand developed to hold the battery at a 45^0 angle in respect to the plane of the thermal detector. This arrangement eliminates the identification of radiation emitted or reflected by the camera and operator. To eliminate reflection from the ceiling and other objects in the environment a large cardboard box was placed over the battery and stand. The camera was situated on a tripod outside the enclosure and pointed such that the detector viewed only the battery inside the box. The lower spread in temperature is seen towards the start of the discharge cycle when contrasted with the intermediate and end of the discharge cycle. Besides, towards the start of the discharge cycle, the differential heating was observed across the cell; the cell heating is biased below cathode (the positive electrode). The positive electrode demonstrates marginally higher temperatures because of the electrical resistivity of the cathode material contrasted with the negative electrode material. The brightest white part in all the images is the range where the most noteworthy temperature distributions are seen and correspondingly the most noteworthy heat generation was expected. This is the expected result when joule heating is the dominant heat generation process. This is because of the concentration of the current as it collects on the "current collector" tabs of the anode and cathode. Additional images at 2C, 3C, and 4C discharge rates are published in [55].

5. Conclusions

This paper has reported a comprehensive investigation of the electrical and thermal performance (temperature profiles at the surface) of a Li-ion battery with $LiFePO_4$ cathode material (20 Ah capacity) at the lower C-rates of C/10, C/5, C/2 and higher C-rates of 1C, 2C, 3C, and 4C. A battery thermal model was created using MATLAB Simulink and the simulated data was validated with the test data for temperature, voltage, heat generation, and internal resistance at all discharge rates of C/10, C/5, C/2, 1C, 2C, 3C, and 4C. The battery thermal model captured the battery thermal behaviour over a wide range of discharge rates (C-rates). It was observed that as the C-rate increased, the surface temperature distributions also increased for all C-rates. The most elevated recorded temperature was observed to be 58.1°C towards the end of the 4C discharge rate (corresponding current was 80A). This implies that the impact of high and low C-rate was studied for this particular battery. In addition, an experimental study was conducted using an IR camera (Flir Therma CAM S60 model) to capture IR images at various discharge rates, and temperature non-uniformity was visually observed. The temperature non-uniformity was an indication of the non-uniformity in the heat generation on a surface of the battery and as such it

was concluded that the area of highest temperature and non-uniformity is the location where the heat generation is highest.

Nomenclature

F	=	Faraday's constant [coulomb/mol]
I	=	Current [A]
n	=	Number of flow of electron
Q	=	Heat generation [J]
$\dot{Q}$	=	Rate of heat generation [W]
R	=	Resistance (Ω)
ΔS	=	Entropy change due to chemical reaction [J/K]
T	=	Temperature [°C or K]
t	=	Time [s]
V	=	Cell voltage or cell potential [V]

Greek Symbol

ζ	=	Heat constant
Ω	=	Ohm

Subscripts

act	=	actual
$batt$	=	battery
chg	=	charge
ct	=	charge transfer
$dchg$	=	discharge
$diff$	=	diffusion
int	=	internal
n	=	negative
oc	=	open circuit
ohm	=	Ohmic
p	=	positive
ss	=	steady state
sim	=	simulated

Acronyms and Abbreviations

3D	Three dimensional
C	Discharge rate
CC	Constant-current
CV	Constant-voltage
DEC	Diethyl carbonate
DMC	Dimethyl carbonate
EC	Ethylene carbonate
EMC	Ethyl-methyl carbonate
EV	Electric vehicle
E-stop	Emergency shutdown
FEM	Finite element model
GUI	Graphical user interface
HEV	Hybrid electric vehicle
I/O	Input/Output
IR	Infra-red
Li-ion	Lithium-ion
LabVIEW	Laboratory virtual instrument engineering workbench
$LiCoO_2$	Lithium cobalt oxide
$LiMn_2O_4$	Lithium manganese oxide
$LiNiMnCoO_2$	Lithium nickel manganese cobalt oxide
$LiFePO_4$	Lithium iron phosphate
LCO	Lithium cobalt oxide
LMO	Lithium manganese oxide
LFP	Lithium phosphate
LPM	Lumped parameter model
LPV	Linear parameter varying
MATLAB	MATrix LABoratory
NN	Neural network
NMC	Lithium manganese cobalt oxide
OCP	Open circuit potential
PC	Personal computer
PDE	Partial differential equation
PHEV	Plug-in hybrid electric vehicle
RC	Resistance capacitance

RS-232	Recommend standard number 232
SOC	State of charge
SEI	Solid electrolyte interface

References

[1] Z. Ling, F. Wang, X. Fang, X. Gao and Z. Zhang, "A hybrid thermal management system for lithium ion batteries combining phase change materials with forced-air cooling," Applied Energy, no. 148, pp. 403-409, 2015.

[2] A. Ritchie and W. Howard, "Recent developments and likely advances in lithium-ion batteries," Journal of Power Sources, vol. 162, pp. 809-812, 2006.

[3] Y. Ye, L. H. Saw, Y. Shi and A. A. Tay, "Numerical analyses on optimizing a heat pipe thermal management system for lithium-ion batteries during fast charging," Applied Thermal Engineering, vol. 86, pp. 281-291, 2015.

[4] R. Abousleiman, A. Al-Refai and O. Rawashdeh, "Charge capacity versus charge time in CC-CV and pulse charging of Li-ion batteries," in SAE International, 2013.

[5] J. Dahn and G. M. Ehrlich, "Lithium-Ion Batteries," in Linden's Handbook of Batteries, New York, McGraw Hill, 2011, pp. 26.1-26.79.

[6] J. Yi, U. S. Kim, C. B. Shin, T. Han and S. Park, "Three-dimensional thermal modeling of a lithium-ion battery considering the combined effects of the electrical and thermal contact resistances between current collecting tab and lead wire," Journal of the Electrochemical Society, vol. 160, no. 3, pp. 437-443, 2013.

[7] J. Zhao, Z. Rao and Y. Li, "Thermal performance of mini-channel liquid cooled cylinder based battery thermal management for cylindrical lithium-ion power battery," Energy Conversion and Management, vol. 103, pp. 157-165, 2015.

[8] Y. Ye, Y. Shi and A. A. Tay, "Electro-thermal cycle life model for lithium iron phosphate battery," Journal of Power Sources, vol. 217, pp. 509-518, 2012.

[9] Y. Xing, Q. Miao, K.-L. Tsui and M. Pecht, "Prognostics and health monitoring for lithium-ion battery," in IEEE International Conference on, 2011.

[10] X. Feng, M. Fang, X. He, M. Ouyang, L. Lu, H. Wang and M. Zhang, "Thermal runaway features of large format prismatic lithium ion battery using extended volume accelerating rate calorimetry," Journal of Power Sources, pp. 255 : 294-301, 2014.

[11] L. Lu, X. Han, J. Hua, M. Ouyang and J. Li, "A review on the key issues for lithium-ion battery management in electric vehicles," Journal of Power Sources, pp. 226:272-288, 2013.

[12] T. Wang, K. J. Tseng, J. Zhao and Z. Wei, "Thermal investigation of lithium-ion battery module with different cell arrangement structures and forced air-cooling strategies," Applied Energy, vol. 134, pp.

229-238, 2014.

[13] W. Waag and D. U. Sauer, "Adaptive estimation of the electromotive force of the lithium-ion battery after current interruption for an accurate state-of-charge and capacity determination," Applied Energy, vol. 111, pp. 416-427, 2013.

[14] L. H. Saw, Y. Ye, A. A. Tay, W. T. Chong, S. H. Kuan and M. C. Yew, "Computational fluid dynamic and thermal analysis of Lithium-ion battery pack with air cooling," Applied Energy, vol. 177, pp. 783-792, 2016.

[15] K. Yeow, M. Thelliez, H. Teng and E. Tan, "Thermal Analysis of a Li-ion Battery System with Indirect Liquid Cooling Using Finite Element Analysis Approach," SAE International Journal, vol. 1, no. 1, pp. 65-78, 2012.

[16] A. Dinger, R. Martin, X. Mosquet, M. Rabl, D. Rizoulis and G. Sticher, "Batteries for Electric Cars,Challenges, Opportunities, and the Outlook to 2020," The Boston Consulting Group, 2010.

[17] L. Y. Shao-Horn, C. Delmas, C. E. Nelson and M. A. O'Keefe, "Atomic resolution of lithium ions in LiCoO2," Nature Materials, vol. 2, pp. 464-467, 2003.

[18] B. Xia, H. Cao, Z. Zhang and N. Xu, "LiAlO2-coated LiCoO2 as cathode material for lithium ion batteries," Solid State Ionics, vol. 176, pp. 911-914, 2005.

[19] A. F. Hollenkamp, A. P. Lewandowski, S. W. Donne and A. S. Best, "Cycling and rate performance of Li-LiFePO4 cells in mixed FSI-TFSI room temperature ionic liquids," Journal of Power Sources, vol. 195, pp. 2029-2035, 2010.

[20] G. X. Wang, S. A. Needham, H. K. Liu and V. A. Drozd, "Synthesis and electrochemical performance of doped LiCoO2 materials," Journal of Power Sources, vol. 174, no. 13th International Meeting on Lithium Batteries., pp. 828-831, 2007.

[21] J. Park, S. Lee, J. Kim, S. Ahn, J.-S. Park and Y. Jeong, "Effect of conducting additives on the properties of composite cathodes for lithium-ion batteries," Journal of Solid State Electrochemistry, vol. 14, no. 4, pp. 593-597, 2010.

[22] C. Julien, "Local Structure of lithiated manganese oxides," Solid State Ionics, vol. 177, pp. 11-19, 2006.

[23] X. He, J. Li, Y. Cai, Y. Wang, J. Ying, C. Jiang and C. Wan, "Preparation of co-doped spherical spinel LiMn2O4 cathode materials for Li-ion batteries," Journal of Power Sources, vol. 150, pp. 216-222, 2005.

[24] J. P. Tu, Y. Z. Yang and W. K. Zhang, "Spray-drying technology for the synthesis of nanosized LiMn2O4 cathode material," Materials Letters, vol. 61, pp. 864-867, 2007.

[25] H.-W. Lee, P. Muralidharan, R. Ruffo, C. M. Mari, Y. Cui and D. K. Kim, "Ultrathin spinel LiMn2O4 nanowires as high power cathode materials for Li-Ion batteries," NANO Letters, vol. 10, no. 10, p. 3852–3856, 2010.

[26] J. T. Bloking, S. Y. Chung and Y. M. Chiang, "Electrically conductive phospho-olivines as lithium storage electrodes," Nature Materials, vol. 1, pp. 123-128, 2002.

[27] R. M. Torresi and F. F. C. Bazito, "Cathodes for lithium ion batteries: the benefits of using nanostructured materials," Journal of the Brazilian Chemical Society, vol. 17, pp. 627-642, 2006.

[28] D. Aurbach, Y. Talyosef, B. Markovsky, E. Markevich, E. Zinigrad, L. Asraf, J. S. Gnanaraj and H.-J. Kim, "Design of electrolyte solutions for Li and Li-ion batteries: a review," Electrochimica Acta, vol. 50, no. 2-3, pp. 247-254, 2004.

[29] R. Xiong, H. He and J. Fan, "Evaluation of Lithium-ion battery equivalent circuit models for state of charge estimation by an experimental approach," Energies, vol. 4, pp. 582-598, 2011.

[30] S. Li, H. Xiaosong and H. Peng, "A comparative study of equivalent circuit models for Li-ion batteries," Journal of Power Sources, vol. 198, pp. 359-367, 2012.

[31] T. Kim and W. Qiao, "A hybrid battery model capable of capturing dynamic circuit characteristics and nonlinear capacity effects," IEEE Transactions on Energy Conversion, vol. 26, pp. 1172-1180, 2011.

[32] M. Ceraolo, T. Huria, J. Gazzarri and R. Jackey, "High fidelity electrical model with thermal dependence for characterization and simulation of high power lithium battery cells," in Electric Vehicle Conference (IEVC),IEEE International, Greenville, 2012.

[33] J. Jiang, H. Ruan, B. Sun, W. Zhang, W. Gao, L. Y. Wang and L. Zhang, "A reduced low-temperature electro-thermal coupled model for lithium-ion batteries," Applied Energy, vol. 177, pp. 804-816, 2016.

[34] J. Jaguemont, L. Boulon and Y. Dubé, "A comprehensive review of lithium-ion batteries used in hybrid and electric vehicles at cold temperatures," Applied Energy, vol. 164, pp. 99-114, 2016.

[35] O. Erdinc, B. Vural and M. Uzunoglu, "A dynamic Lithium-ion Battery Model Considering the Effects of Temperature and Capacity Fading, Clean Electrical Power," in International Conference, IEEE, pp. 383–386., 2009.

[36] L. Lam, P. Bauer and E. Kelder, "A Practical Circuit-Based Model for Li-ion Battery Cells in Electric Vehicle Applications," in In Telecommunications Energy Conference (INTELEC), IEEE 33rd International, pp. 1–9., 2011.

[37] A. Ostadi, M. Kazerani and S. K. Chen, "Optimal Sizing of the Energy Storage System (ESS) in a Battery-Electric Vehicle," Transportation Electrication Conference and Expo (ITEC), IEEE, pp. 1-6, 2013.

[38] S. Panchal, I. Dincer, M. Agelin-Chaab, R. Fraser and M. Fowler, "Experimental and theoretical investigation of temperature distributions in a prismatic lithium-ion battery," International Journal of Thermal Sciences, vol. 99, pp. 204-212, 2016.

[39] S. Panchal, I. Dincer, M. Agelin-Chaab, R. Fraser and M. Fowler, "Thermal modeling and validation of temperature distributions in a prismatic lithium-ion battery at different discharge rates and varying

boundary conditions," Applied Thermal Engineering, vol. 96, pp. 190-199, 2016.

[40] S. Panchal, I. Dincer, M. Agelin-Chaab, R. Fraser and M. Fowler, "Experimental and theoretical investigations of heat generation rates for a water cooled LiFePO4 battery," International Journal of Heat and Mass Transfer, vol. 101, pp. 1093-1102, 2016.

[41] S. Panchal, I. Dincer, M. Agelin-Chaab, R. Fraser and M. Fowler, "Experimental investigation and simulation of temperature distributions in a 16Ah-LiMnNiCoO2 battery during rapid discharge rates," Heat and Mass Transfer, pp. 1-10, 2016.

[42] A. Pruteanu, B. V. Florean, G. Maria Moraru and R. C. Ciobanu, "Development of a thermal simulation and testing model for a superior lithium-ion-polymer battery," in Optimization of Electrical and Electronic Equipment (OPTIM), IEEE, pages 947–952, 2012.

[43] C. Alaoui, "Solid-State Thermal Management for Lithium-Ion EV Batteries," Vehicular Technology, IEEE Transactions on, vol. 62, no. 1, pp. 98-107, 2013.

[44] X. Hu, S. Asgari, S. Lin, S. Stanton and W. Lian, "A linear parameter-varying model for HEV/EV battery thermal modeling," in Energy Conversion Congress and Exposition (ECCE), IEEE, pages 1643-1649, 2012.

[45] A. Smyshlyaev, M. Krstic, N. Chaturvedi, J. Ahmed and A. Kojic, "PDE model for thermal dynamics of a large," in American Control Conference (ACC), IEEE, pages 959-964, 2011.

[46] M. A. Keyser, A. Pesaran and M. Mihalic, "Thermal Characterization of Advanced Lithium-Ion Polymer Cells," in Third Advanced Automotive Battery Conference, 2003.

[47] M.-C. Niculuta and C. Veje, "Analysis of the thermal behavior of a LiFePO4," Journal of Physics: Conference Series, vol. 395, 2012.

[48] C. R. Pals and J. Newman, "Thermal modeling of the lithium/polymer battery," Journal of the Electrochemical Society, vol. 142, no. 10, pp. 3274-3281, 1995.

[49] Y. Chen and J. W. Evans, "Three-dimensional thermal modeling of lithium-polymer batteries under galvanostatic discharge and dynamic power profile," Journal of the Electrochemical Society, vol. 141, no. 11, pp. 2947-2952, 1994.

[50] G. Wierschem, B. McKinney and E. Nrotek, "Thermal management of lead-acid batteries for electric vehicles," in Research and developement testing, Detroit, 1993.

[51] A. A. Pesaran, A. Vlahinos and S. D. Burch, "Thermal performance of EV and HEV battery modules and packs," National Renewable Energy Laboratory, Golden, Colorado, 1997.

[52] K. Smith and C.-Y. Wang, "Power and thermal characterization of a lithium-ion battery pack for hybrid-electric vehicles," Journal of Power Sources, vol. 160, no. 1, pp. 662-673, 2006.

[53] W. B. Gu and C. Y. Wang, "Thermal-electrochemical modeling of battery systems," Journal of The Electrochemical Society, vol. 147, no. 8, pp. 2910-2922, 2000.

[54] H. He, R. Xiong and J. Fan, "Evaluation of Lithium-Ion Battery Equivalent Circuit Models for State of Charge Estimation by an Experimental Approach," Energies, vol. 4, no. 4, pp. 582-598, 2011.

[55] S. Panchal, S. Mathewson, R. Fraser, R. Culham and M. Fowler, "Thermal Management of Lithium-Ion Pouch Cell with Indirect Liquid Cooling using Dual Cold Plates Approach," SAE International, vol. 4, no. 2, 2015.

List of Table Captions

List of Figure Captions

Tables

Table 1 : $LiFePO_4$- 20Ah Li-ion prismatic pouch cell specifications

Specifications	Value
Cathode Material	$LiFePO_4$
Anode Material	Graphite
Electrolyte	Carbonate based
Nominal Capacity	20.0 Ah
Nominal Voltage	3.3 V
Dimensions	7.25 mm x 160 mm x 227 mm

Table 2 : Selected discharge rates and corresponding currents

Discharge Rate	Constant Current
C/10	2 A
C/5	4 A
C/2	10 A
1C	20 A
2C	40 A
3C	60 A
4C	80 A

Table 3 : Summary of maximum temperatures and discharge capacities at each discharge rate

C-Rate	Maximum Temperature	Discharge Capacity
C/10	21.8°C	19.30 Ah
C/5	23.7°C	19.46 Ah
C/2	24°C	19.47 Ah
1C	27.8°C	19.44 Ah
2C	35.6°C	19.33 Ah
3C	46°C	19.21 Ah
4C	58.1°C	19.22 Ah

Figures

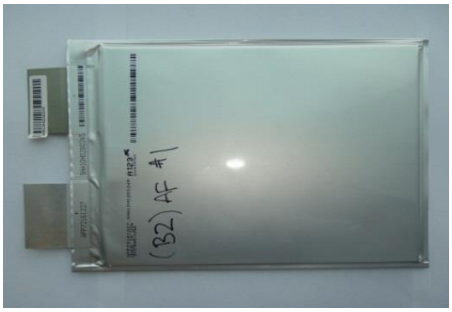

Figure 1 : A picture of a LiFePO4- 20Ah Li-ion prismatic pouch cell

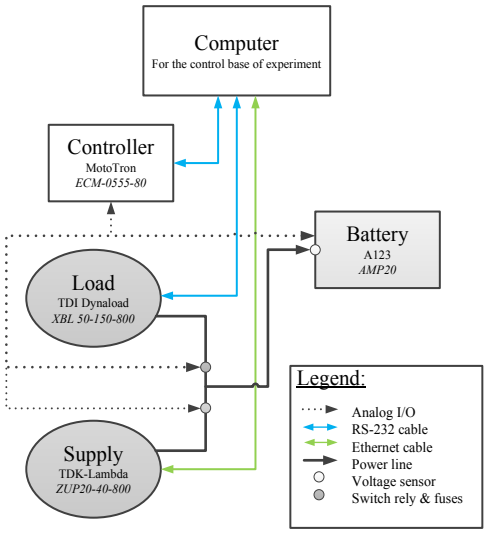

Figure 2 : Schematic of experimental set-up

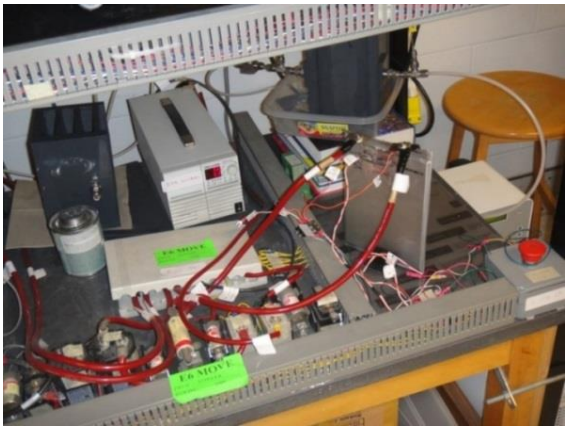

Figure 3 : Picture of the battery set-up

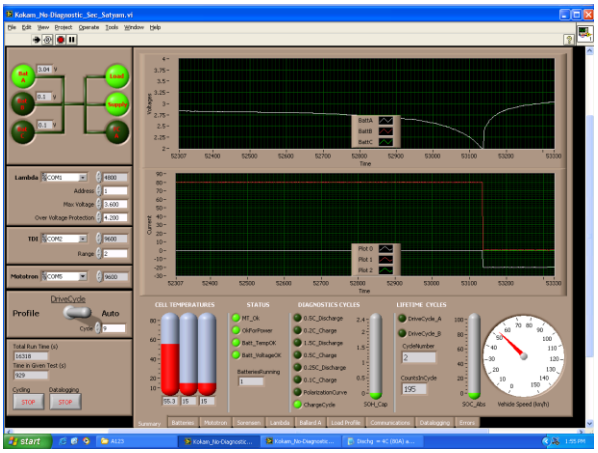

Figure 4 : Screen capture of LabVIEW interface

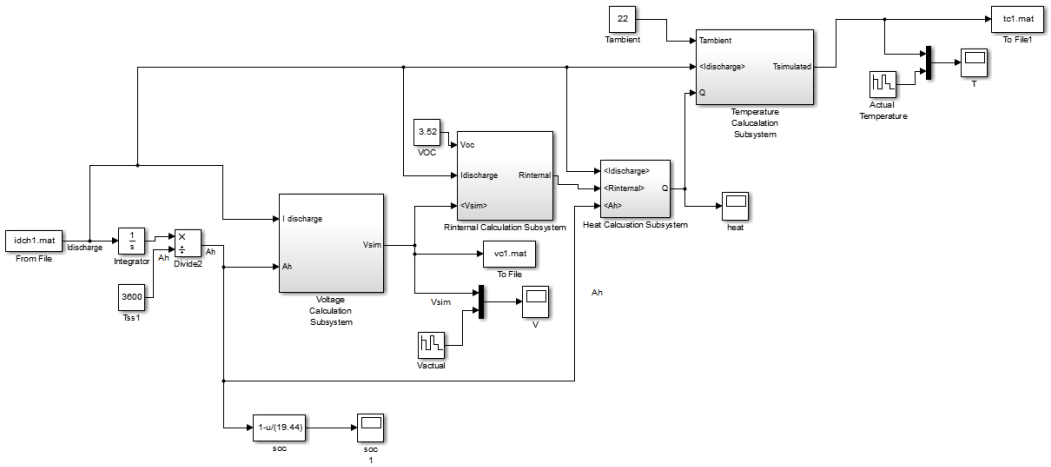

Figure 5 : MATLAB Simulink block diagram

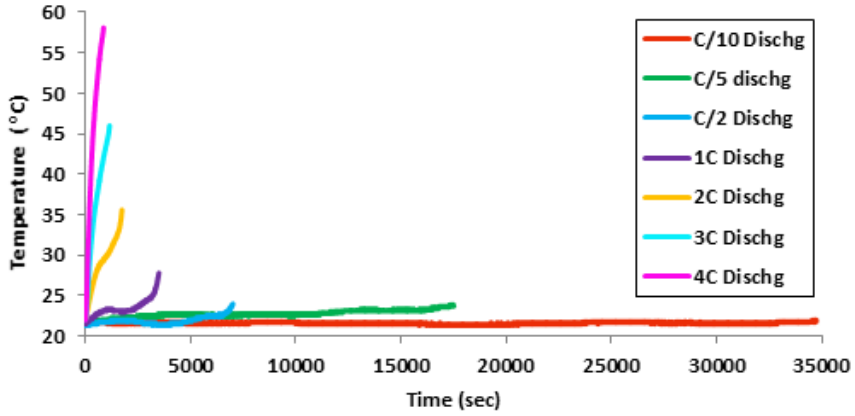

Figure 6 : Battery surface temperature profiles during discharging at C/10, C/5, C/2, 1C, 2C, 3C, and 4C

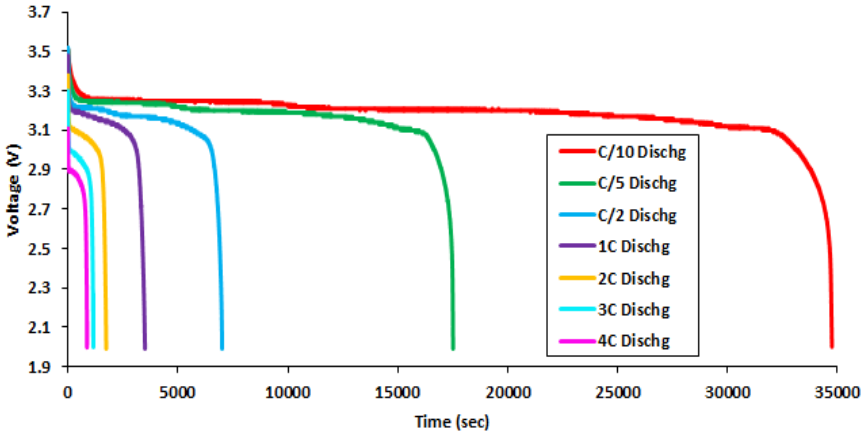

Figure 7 : Battery voltage profiles during discharging at C/10, C/5, C/2, 1C, 2C, 3C, and 4C

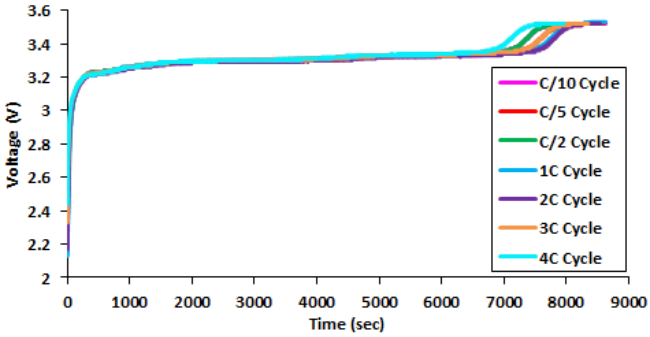

Figure 8 : Battery voltage profiles during charging at C/10, C/5, C/2, 1C, 2C, 3C, and 4C

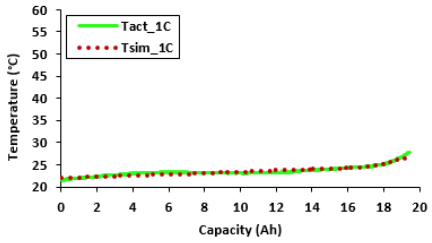

(a) Tempreature profile at 1C

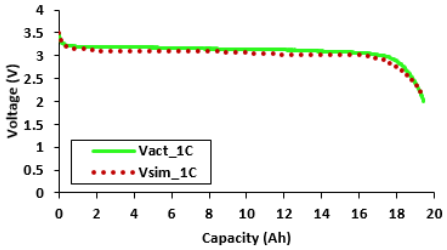

(e) Voltage profile at 1C

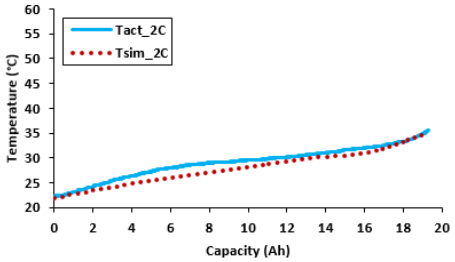

(b) Tempreature profile at 2C

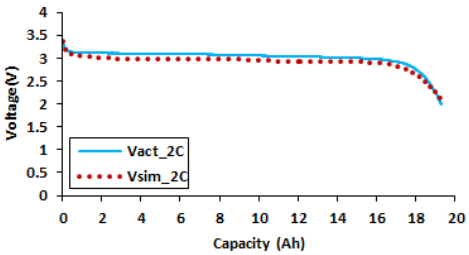

(f) Voltage profile at 2C

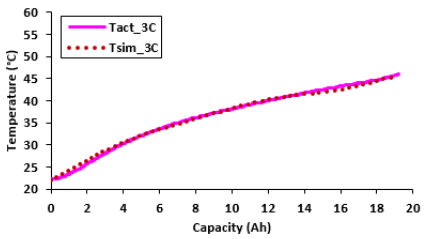

(c) Tempreature profile at 3C

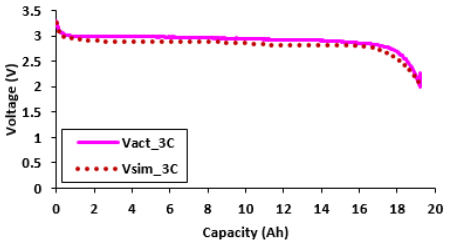

(g) Voltage profile at 3C

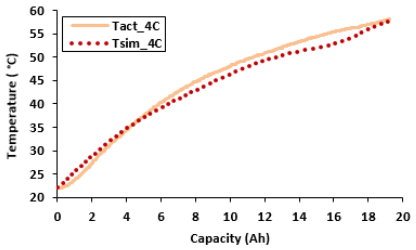

(d) Tempreature profile at 4C

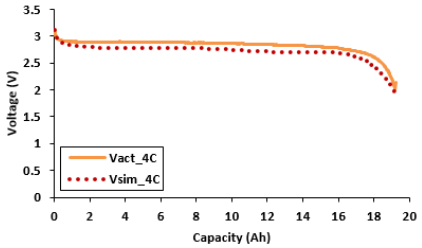

(h) Voltage profile at 4C

Figure 9 : Experimental and simulated temperature and voltage profiles at 1C, 2C, 3C and 4C

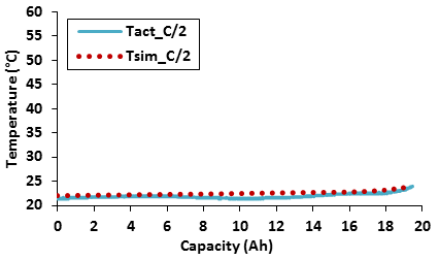

(a) Tempreature profile at C/2

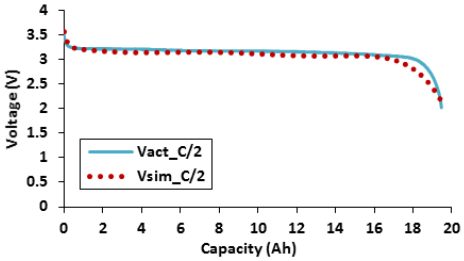

(d) Voltage profile at C/2

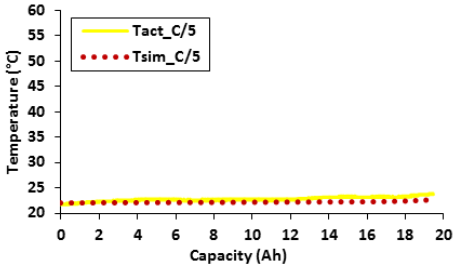

(b) Tempreature profile at C/5

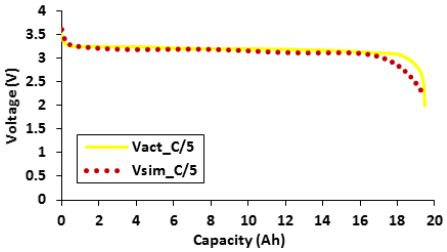

(e) Voltage profile at C/5

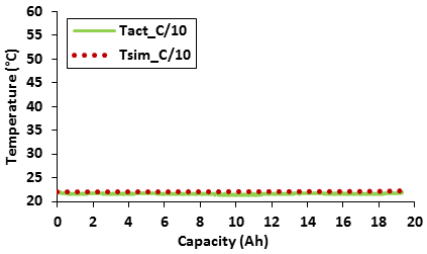

(c) Tempreature profile at C/10

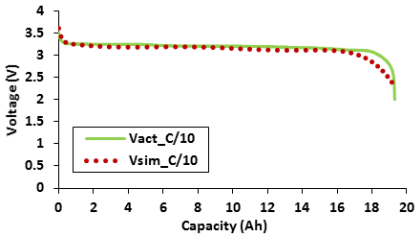

(f) Voltage profile at C/10

Figure 10 : Experimental and simulated temperature and voltage profiles at C/2, C/5 and C/10

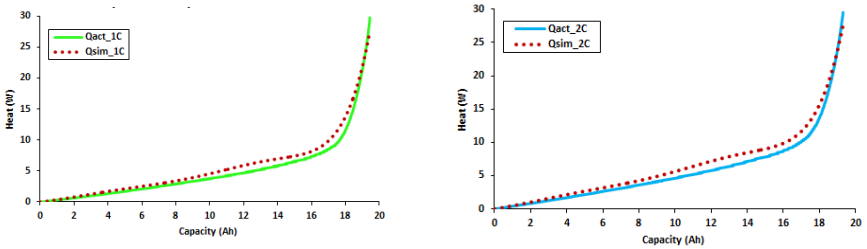

(a) Heat generation rate at 1C

(b) Heat generation rate at 2C

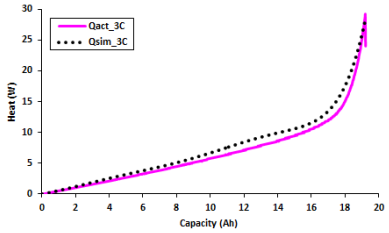

(c) Heat generation rate at 3C

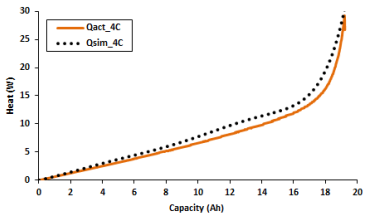

(d) Heat generation rate at 4C

Figure 11 : Experimental and simulated heat generation rate at 1C, 2C, 3C and 4C

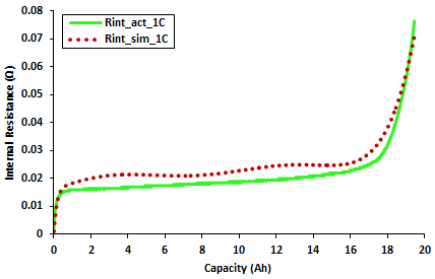

(a) Internal resistance at 1C

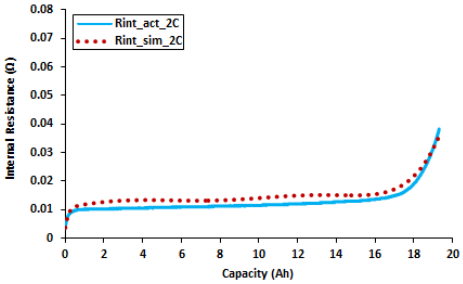

(b) Internal resistance at 2C

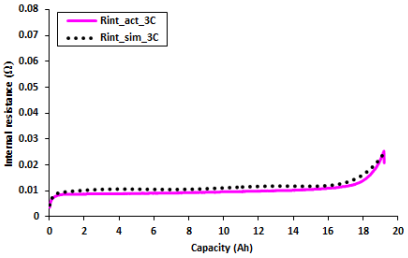

(c) Internal resistance at 3C

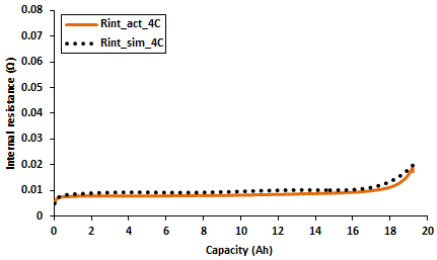

(d) Internal resistance rate at 4C

Figure 12 : Experimental and simulated internal resistance at 1C, 2C, 3C and 4C

Figure 13 : Flir Therma CAM S60 during IR image

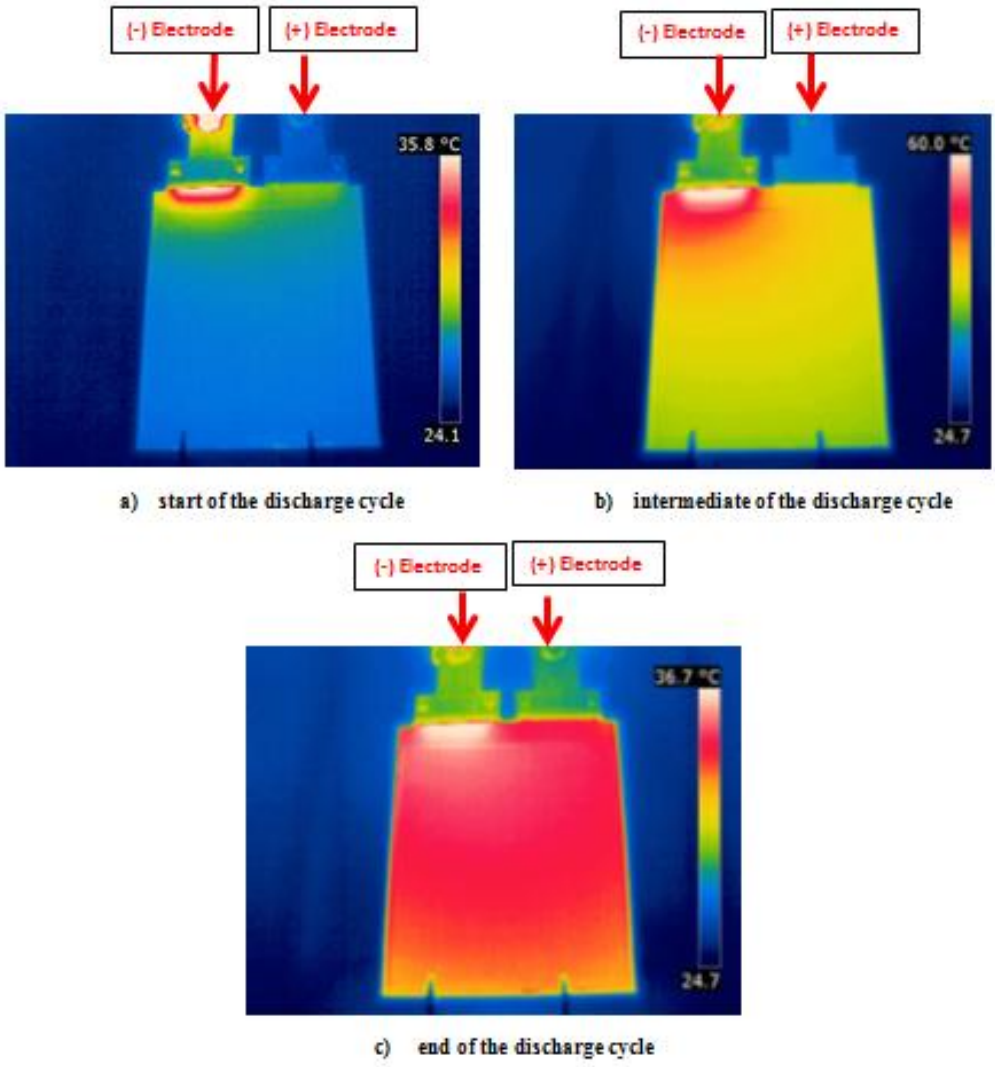

Figure 14 : Thermal images at the start (a), intermediate (b) and at the end (c) of discharge during discharge of 4.5C